

defined in these mutants. Similarly, disruption of Fz signalling did not perturb the orthogonal orientation of pIIb division and Numb localization relative to its sister cells (Fig. 3c). Thus, characteristic perpendicular pairs of cell clusters were observed in *fz* and *dsh* mutant, as in wild-type, pupae (Fig. 3d–f, i).

These data show that the orientation of the pIIa and pIIb divisions is not determined by Fz-mediated tissue polarity. They further indicate that the axis of pI division and/or the relative position of its daughter cells regulates the orientation of the pIIa and pIIb divisions. Two observations are consistent with this conclusion. First, the variability in angle values for pIIa division was larger than that seen for pI, as if it resulted from the addition of its own variability and those observed for pI (Fig. 1b, d). Second, the variability in angle values for pIIb division is lower when angles were measured relative to pIIa daughter cells ($80 \pm 22^\circ$; Fig. 1f) than when they were measured relative to the notum midline ($75 \pm 35^\circ$).

Our results indicate that the polarity of the three mitotic cells in the bristle lineage are regulated by distinct mechanisms. The polarity of pI is regulated by Fz signalling. Fz seems to specifically regulate the orientation of pI divisions, as epidermal cell divisions were not spatially orientated in the notum (results not shown). In contrast to pI, the orientations of the pIIa and pIIb divisions are independent of Fz signalling and, instead, are defined by the axis of the previous pI division. This could be either through positioned cortical marks, as described for yeast¹⁶, or through cell–cell signalling between sister cells.

Studies of neuroblast divisions in the embryo indicate that Inscuteable (Insc) coordinates both the orientation of mitotic spindles and the position of the Numb crescent¹⁷. As the mitotic spindle and the Numb crescent are both misorientated in a coordinated manner in *fz* and *dsh* mutant pI cells, we propose that Fz signalling controls the localization and/or the activity of an organizer acting similarly to Insc in pI. Insc is unlikely to be such a pI organizer because clonal analysis shows that *insc* regulates neither bristle differentiation nor polarity in the notum (not shown). Similarly, in the embryo, *insc* activity appears to be dispensable in mitotic sense-organ cells that have a planar polarity¹⁷. Insc may thus act primarily in apicobasal polarity in epithelial cell. The organizer acting downstream of Fz signalling in planar divisions remains to be identified.

Control of cell polarity by Fz signalling has been evolutionarily conserved, at least from nematodes to flies^{18–20}. However, the *mom-5* and *lin-17* genes, which encode Fz-like receptors in *Caenorhabditis elegans*, are required to establish both orientation of division and asymmetry, whereas *fz* is required to regulate the orientation, but not the asymmetry, of pI divisions. Whether Fz signalling also contributes to determining cell polarity during asymmetric divisions in vertebrates is unknown. □

Methods

Drosophila stocks. The A101 line carries a P[*lacZ*, *ry*⁺] enhancer-trap allele of *neuralised* that specifically expresses nuclear β -galactosidase in pI and its progeny cells²¹. The dA-10 transformant line carries a *deadpan-lacZ* construct expressing cytoplasmic β -galactosidase in pI and its progeny cells²² (gift from E. Bier). The following mutant alleles were used: *dsh*¹, *fr*²⁵⁴, *fz*^{K21} and *fz*^{KDaa} (gifts from F. Chanut, D. Coen and P. Adler). Lineage analysis was conducted in A101/TM6b, dA-10, *fz*^{K21}/*fz*^{KDaa}, dA-10; *fz*²⁵⁴, *dsh*¹; A101/+. The hs-Nintra/CyO transformant line I4A (gift from T. Lieber) was used to overexpress an activated form of Notch (for 30 min at 37°C).

Immunostaining. Dissected nota from pupae at 16–24 h APF were processed as described⁷. Primary antibodies were rabbit anti-Numb (gift from Y.-N. Jan; 1:1000); mouse anti- β -galactosidase (Promega; 1:2000); rat anti- α -tubulin (Serotec; 1:3000); rat anti-Su(H) (1:500), mouse anti-Prospero (MR1A, gift from C. Doe; 1/2), mouse anti-Cut (2B10, DSHB; 1:500) and rabbit anti- β -galactosidase (Cappel; 1:500). Secondary conjugated antibodies were: Indodicarbocyanine-anti-rabbit (Jackson; 1:500); Indodicarbocyanine-anti-mouse (Jackson; 1:500); fluorescein-isothiocyanate-anti-rat (Jackson; 1:100); lissa-

mine rhodamine sulphonyl chloride-anti-mouse (Jackson; 1:200); tetramethyl rhodamine isothiocyanate anti-rabbit (Biosys; 1:200). Confocal images were obtained on a Leica TCS 4D confocal microscope and images were processed with NIH images and Photoshop programs.

Received 19 November 1997; accepted 10 March 1998.

- Horvitz, H. & Herskowitz, I. Mechanisms of asymmetric cell division: two Bs or not two Bs, that is the question. *Cell* **68**, 237–255 (1992).
- Hartenstein, V. & Posakony, J. W. Development of adult sensilla on the wing and notum of *Drosophila melanogaster*. *Development* **107**, 398–405 (1989).
- Rhyu, M. S., Jan, L. Y. & Jan, Y. N. Asymmetric distribution of Numb protein during division of the sensory organ precursor cell confers distinct fates to daughter cells. *Cell* **76**, 477–491 (1994).
- Knoblich, J. A., Jan, L. Y. & Jan, Y. N. Asymmetric segregation of Numb and Prospero during cell division. *Nature* **377**, 624–627 (1995).
- Frise, E., Knoblich, J. A., Younger-Shepherd, S., Jan, L. Y. & Jan, Y. N. The *Drosophila* Numb protein inhibits signaling of the Notch receptor during cell-cell interaction in sensory organ lineage. *Proc. Natl Acad. Sci. USA* **93**, 11925–11932 (1996).
- Guo, M., Jan, L. Y. & Jan, Y. N. Control of daughter cell fates during asymmetric division: interaction of Numb and Notch. *Neuron* **17**, 27–41 (1996).
- Gho, M., Lecourtis, M., Géraud, G., Posakony, J. W. & Schweisguth, F. Subcellular localization of Suppressor of Hairless in *Drosophila* sense organ cells during Notch signalling. *Development* **122**, 1673–1682 (1996).
- Wang, S., Younger-Shepherd, S., Jan, L. Y. & Jan, Y. N. Only a subset of binary cell fate decisions mediated by Numb/Notch signaling in *Drosophila* sensory organ lineage requires *Suppressor of Hairless*. *Development* **124**, 4435–4446 (1997).
- Lawrence, P. A. Gradients in the insect segment: the orientation of hairs in the milkweed bug *Oncopeltus fasciatus*. *J. Exp. Biol.* **44**, 607–620 (1996).
- Bate, C. M. in *Handbook of Sensory Physiology* (ed. Jakobson, M.) 1–52 (Springer, Berlin, 1978).
- Lieber, T., Kidd, S., Alcano, E., Corbin, V. & Young, M. W. Antineurogenic phenotypes induced by truncated Notch proteins indicate a role in signal transduction and may point to a novel function for Notch in nuclei. *Genes Dev.* **7**, 1949–1965 (1993).
- Adler, P. N. The genetic control of tissue polarity in *Drosophila*. *Bioessays* **14**, 735–741 (1992).
- Park, W.-J., Lin, J. & Adler, P. N. The *frizzled* gene of *Drosophila* encodes a membrane protein with an odd number of transmembrane domains. *Mech. Dev.* **45**, 127–137 (1994).
- Krasnow, R. E., Wong, L. L. & Adler, P. N. *dishevelled* is a component of the *frizzled* signaling pathway in *Drosophila*. *Development* **121**, 4095–4102 (1996).
- Jones, K. H., Lin, J. & Adler, P. N. Molecular analysis of EMS-induced *frizzled* mutations in *Drosophila melanogaster*. *Genetics* **142**, 205–215 (1996).
- Gonczy, P. & Hyman, A. Cortical domains and the mechanisms of asymmetric cell division. *Trends Cell Biol.* **6**, 382–387 (1996).
- Kraut, R., Chia, W., Jan, L. Y., Jan, Y. N. & Knoblich, J. A. Role of *inscuteable* in orientating asymmetric cell divisions in *Drosophila*. *Nature* **383**, 50–55 (1996).
- Thorpe, C. J., Schlesinger, A., Clayton Carter, J. & Bowerman, B. Wnt signaling polarizes an early *C. elegans* blastomere to distinguish endoderm from mesoderm. *Cell* **90**, 695–705 (1997).
- Rocheleau, C. et al. Wnt signaling and an APC-related gene specify endoderm in early *C. elegans* embryos. *Cell* **90**, 707–716 (1997).
- Sawa, H., Lobel, L. & Horvitz, H. R. The *Caenorhabditis elegans* lin-17, which is required for certain asymmetric cell division, encodes a putative seven-transmembrane protein similar to the *Drosophila* Frizzled protein. *Genes Dev.* **10**, 2189–2197 (1996).
- Usui, K. & Kimura, K. Sequential emergence of the evenly spaced microchaetes on the notum of *Drosophila*. *Arch. Dev. Biol.* **203**, 151–158 (1993).
- Emery, J. F. & Bier, E. Specificity of CNS and PNS regulatory subelements comprising pan-neural enhancers of the *deadpan* and *scratch* genes is achieved by repression. *Development* **121**, 3549–3560 (1995).

Acknowledgements. We thank P. Adler, E. Bier, D. Coen, F. Chanut, C. Doe, Y.-N. Jan, T. Lieber and the Developmental Studies Hybridoma Bank for flies and antibodies; F. Rosa and M. Wassef for critical reading of the manuscript; and the Imaging facility of the Institut Jacques Monod for use of confocal microscopes. This work was supported by grants from the CNRS, the MENESR, the Fondation pour la Recherche Médicale, the Association pour la Recherche contre le Cancer and the Ligue Nationale contre le Cancer—Comité de Paris.

Correspondence and requests for materials should be addressed to M.G. (e-mail: mgbo@wotan.ens.fr).

The molecular elasticity of the extracellular matrix protein tenascin

Andres F. Oberhauser, Piotr E. Marszalek, Harold P. Erickson* & Julio M. Fernandez

Department of Physiology and Biophysics, Mayo Foundation, Rochester, Minnesota 55905, USA

* Department of Cell Biology, Duke University Medical Center, Durham, North Carolina 27710, USA

Extracellular matrix proteins are thought to provide a rigid mechanical anchor that supports and guides migrating and rolling cells^{1–4}. Here we examine the mechanical properties of the extracellular matrix protein tenascin by using atomic-force-microscopy techniques. Our results indicate that tenascin is an

elastic protein. Single molecules of tenascin could be stretched to several times their resting length. Force–extension curves showed a saw-tooth pattern, with peaks of force at 137 pN. These peaks were ~25 nm apart. Similar results have been obtained by study of titin⁵. We also found similar results by studying recombinant tenascin fragments encompassing the 15 fibronectin type III domains of tenascin. This indicates that the extensibility of tenascin may be due to the stretch-induced unfolding of its fibronectin type III domains. Refolding of tenascin after stretching, observed when the force was reduced to near zero, showed a double-exponential recovery with time constants of 42 domains refolded per second and 0.5 domains per second. The former speed of refolding is more than twice as fast as any previously reported speed of refolding of a fibronectin type III domain^{6,7}. We suggest that the extensibility of the modular fibronectin type III region may be important in allowing tenascin–ligand bonds to persist over long extensions. These properties of fibronectin type III modules may be of widespread use in extracellular proteins containing such domain^{8,9}.

Tenascins are extracellular matrix proteins that are conserved in all vertebrates^{10,11}. Their functional roles include cell adhesion and the consequent mechanical interactions between cells. These proteins are typically disulphide-linked hexamers called hexabrachions. Each tenascin subunit is made up of a series of repeated structural domains, including tandem epidermal growth factor (EGF)-like repeats, tandem fibronectin type III (FN-III) domains and a terminal knob region homologous to a region of fibrinogen^{10,11}. Tenascin mediates the attachment and rolling of cells in shear flow¹². The attachment site on tenascin is the terminal knob, which binds to an unknown receptor on the rolling cells. A significant feature of tenascin is that the splice variants differ only in the number of FN-III repeats (8–15), indicating that the tandem FN-III modules may have a functional role that is finely regulated^{10,11}.

The FN-III domain is a common motif of modular proteins and is found in ~2% of all animal proteins¹³. The FN-III domain is characterized by its folding into a seven-stranded β -barrel, a structure that is very similar to that of immunoglobulin domains^{8,14}. The tandem repeats of immunoglobulin domains of the giant

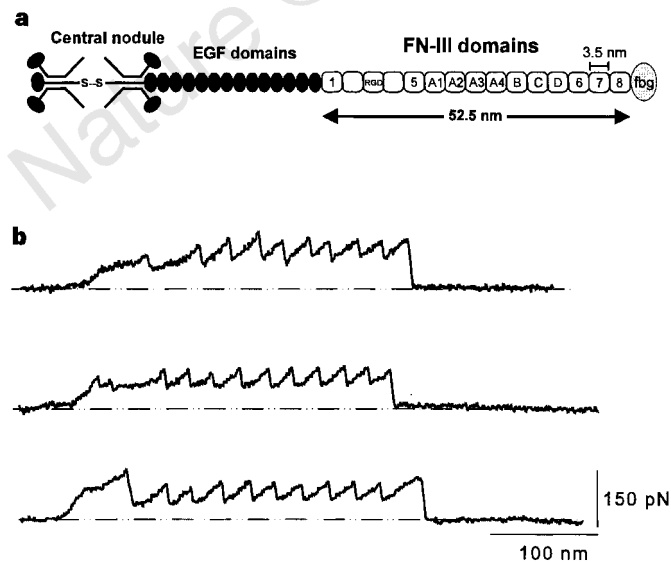


Figure 1 Force–extension relationships for native tenascin hexabrachions measured with AFM techniques. **a**, Modular construction of one subunit of the hexameric tenascin^{10,11}. The EGF domains of tenascin have internal disulphide bonds (S–S) that prevent extension¹¹. Extension of tenascin involves unfolding FN-III domains, and perhaps part of the central knob. (RGD, single-letter amino-acid code; fbg, fibrinogen.) **b**, Stretching single hexabrachions gave force–extension curves that followed a saw-tooth pattern with equally spaced force peaks.

muscle protein titin function as an extensible shock absorber with hysteresis^{5,15–17}. The elastic properties of the tandem immunoglobulin region of titin are due to the forced unfolding of individual immunoglobulin domains. In the atomic-force-microscope (AFM) experiments, rapid unfolding was seen when the immunoglobulin domains were strained by forces of up to 300 pN (ref. 5). It seemed likely that the tandem FN-III domains of tenascin could also act as an extensible segment in the mechanical interactions of tenascin with cells and extracellular matrix.

We have used AFM techniques^{5,18–20} to examine the mechanical properties of the human tenascin-C protein (Fig. 1). We used the large splice variant of tenascin-C which has 15 FN-III domains per subunit²¹. The protein was adsorbed onto a gold-coated coverslip and placed in the recording chamber of a single-axis AFM. Random segments of tenascin-C were picked up by an AFM tip and then stretched. The resulting force–extension curves showed a saw-tooth pattern, with as many as 12 peaks with an average force of 137 ± 12 pN ($n = 42$; pulling speed, $0.2\text{--}0.6$ nm ms⁻¹). The force peaks were equally spaced by a distance of 24.8 ± 2.3 nm ($n = 37$). A unique feature of the tenascin force–extension curves is a ‘hump’ that precedes the first force peak. Incubating tenascin with the

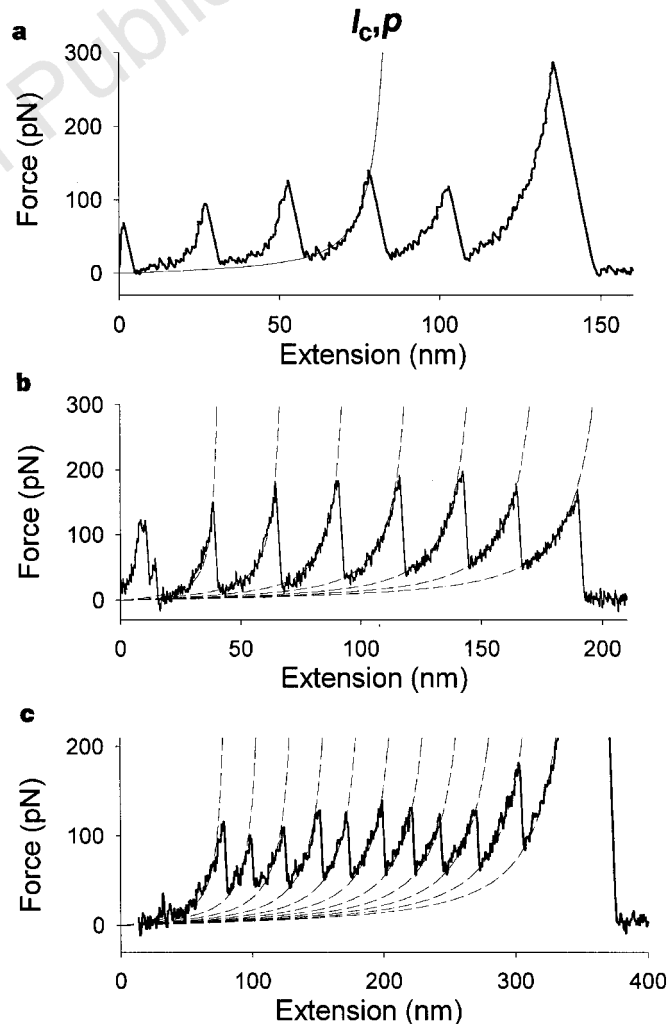


Figure 2 The WLC model, using a persistence length of $p = 0.42$ nm and a contour length increment of $\Delta l_c = 28.5$ nm, describes the force–extension curves of recombinant tenascin fragments. **a**, Force–extension curve for a TNfnA-D protein. The smooth curve corresponds to the fit of an individual force–extension peak to the WLC equation $F(x) = kT/p(x/l_c + 1/4(1 - x/l_c)^2 - 1/4)$. **b**, **c**, A family of WLC curves generated with the parameters found in **a** describes the force–extension curves of the TNfnALL protein (**b**; dotted lines) and of native dithiothreitol-treated tenascin (**c**; dotted lines).

reducing reagent dithiothreitol (1 mM for 1 h, a treatment that disrupts the hexabrachion into single arms; H.P.E., unpublished data) eliminated the hump. This hump may therefore result from stretching the α -helical and central knob domains of the native hexabrachion.

We also studied the recombinant tenascin segment TNfnALL²¹, which is composed of 15 FN-III domains and corresponds to the largest splice variant, and TNfnA-D²¹, which is made of seven FN-III domains and corresponds to one of the spliced segments in native tenascin. Stretching the recombinant proteins TNfnALL and TNfnA-D produced saw-tooth-like force-extension curves (Fig. 2).

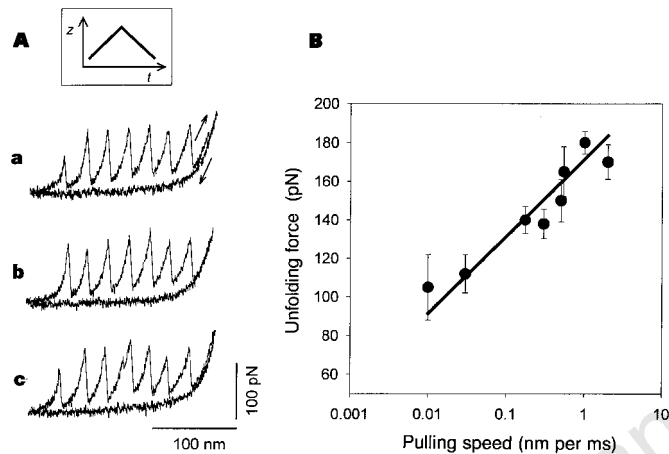


Figure 3 Repeated unfolding/refolding cycles of a single recombinant TNfnALL protein. **A**, Three consecutive unfolding/refolding cycles separated by 5 s (**a**, **b**) and 15 s (**b**, **c**). **a**, Upwards arrow indicates extension and downwards arrow indicates relaxation. **B**, Dependence of the unfolding forces on pulling speed. The filled circles show the result of five different experiments ($n = 191$). The solid line is the result of a Monte Carlo simulation of the speed dependency of the force peaks measured during the simulated unfolding of ten FN-III domains placed in series. The inset shows z-axis motion as a function of time.

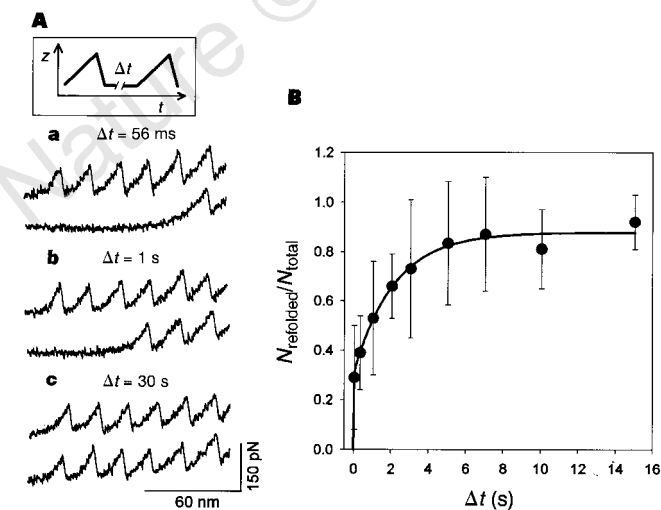


Figure 4 Repeated refolding cycles of a single TNfnAll protein using a double-pulse experiment (inset) identifies at least two refolding rate constants. **A**, A first extension identifies the total number of domains that unfold, N_{total} . (**a-c**, top traces). Then, the protein is relaxed to its resting length to allow refolding. After a delay, Δt , a second extension measures the number of refolded domains, N_{refolded} (**a-c**, bottom traces). **B**, Plot of $N_{\text{refolded}}/N_{\text{total}}$ versus Δt . Each symbol is the average of (from left to right) 79, 40, 45, 22, 12, 3, 14 and 6 data points obtained from 4 separate experiments. The solid line is a two-exponential fit of the data to the function $N_{\text{refolded}}/N_{\text{total}} = A_1(1 - e^{-\Delta t/\beta_{01}}) + A_2(1 - e^{-\Delta t/\beta_{02}})$, where $A_1 = 0.3$, $A_2 = 0.57$, $\beta_{01} = 42 \text{ s}^{-1}$ and $\beta_{02} = 0.5 \text{ s}^{-1}$.

The force peaks of TNfnALL and TNfnA-D had an average force of $138 \pm 50 \text{ pN}$ ($n = 146$; pulling speed, $0.3\text{--}0.5 \text{ nm ms}^{-1}$) and a spacing of $24.7 \pm 1.2 \text{ nm}$.

The elasticity of a polypeptide chain is well described by the worm-like-chain (WLC) model, which predicts the relationship between the extension of a polymer and the entropic restoring force generated^{5,16,17}. The adjustable parameters of the WLC model are the persistence length, p , and the contour length of the polymer, l_c (see ref. 22 for a complete description). Nonlinear fits (Levenberg-Marquardt fits) of the WLC function to the force-extension curves that lead to each force peak showed that the WLC model adequately describes the elasticity of stretched tenascin (Fig. 2a, solid line). The fits gave an average persistence length of $p = 0.42 \pm 0.22 \text{ nm}$ ($n = 75$). The contour length determined by the fits ranged from 25 nm to 496 nm. However, the change in contour length between consecutive force peaks was a constant, $\Delta l_c = 28.5 \pm 4.0 \text{ nm}$ ($n = 96$). A family of WLC curves generated with a persistence length of 0.42 nm and contour length increments of 28.5 nm describes well the force-extension curves of the recombinant tenascin protein TNfnALL (Fig. 2b) and of native tenascin (Fig. 2c).

The size of a folded tenascin FN-III domain was estimated from the crystal structure to be 3.6 nm (ref. 23). The tenascin FN-III domains consist of between 88 and 92 amino acids. When the

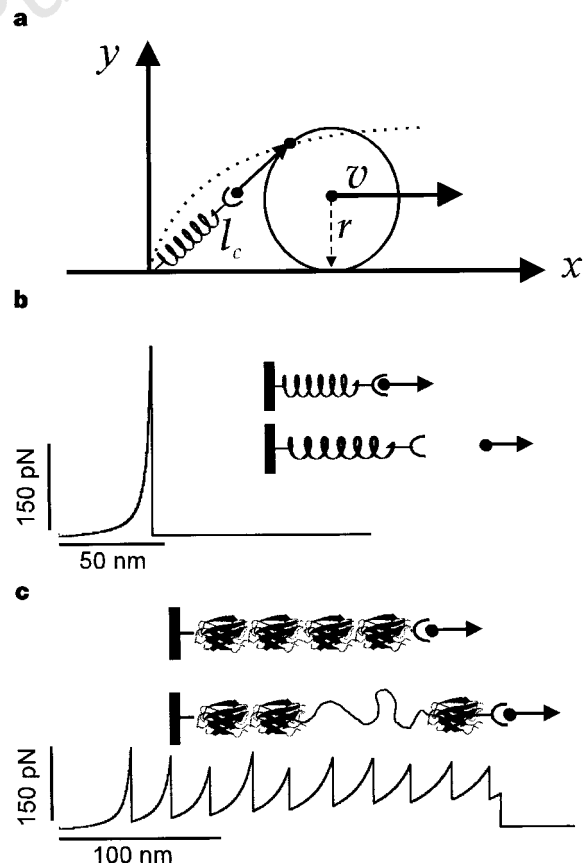


Figure 5 A Monte Carlo simulation shows that tandem FN-III repeats can extend the range and lifetime of a protein-ligand bond and reduce the force required to break it (see Methods). **a**, During cell rolling, a protein bound to a cell ligand is stretched along a cycloidal path (dotted line). The protein is represented by a coil and the ligand by a black circle near to the coil. **b**, Simulation of a bound 50-nm-long protein, without extensible modules, stretched at a speed of 0.2 nm ms^{-1} , predicts a force-extension curve where bond breakage occurs after a 45-nm extension and at a force of 330 pN. **c**, At the same pulling speed, the simulated force-extension curve of a cell-bound protein composed of 15 FN-III domains (inset; only four are shown) shows bond breakage after an extension of 268 nm and at 69 pN.

polypeptide is maximally extended, each amino acid contributes 0.38 nm to the contour length, so unfolding a domain could lengthen the subunit by 31 nm. This is slightly more than the observed increase of 28.5 nm and implies that extension to 90% of maximum requires a force sufficient to unfold the next domain.

We could stretch and relax a protein repeatedly if we limited the extension so that the molecule did not detach from the AFM tip or the substrate. Under these conditions, we observed that extension always showed the saw-tooth pattern of unfolding, whereas relaxation showed a monotonic force–relaxation curve (Fig. 3A). Repeated extension–relaxation curves showed a similar pattern, showing that unfolding was fully reversible. Refolding could not be observed during the force–relaxation curve, indicating that domain refolding may not have begun until the protein was relaxed to, or near to, its original length (Fig. 3A). There should be some small force associated with the refolding, but it is too small to measure with our instrument.

The rate of extension of a tenascin protein is an important factor determining the peak forces at which unfolding was observed. We examined this by varying the pulling speed over a wide range (0.01–2 nm ms⁻¹). A 100-fold reduction in the pulling speed reduced the unfolding force by ~75 pN (Fig. 3B). The speed dependence of the unfolding force is well described by a Monte Carlo simulation that assumes a two-state model for the folding/unfolding reaction (Fig. 3B, solid line). In this simulation, we used the unfolding length that was found for the titin immunoglobulin modules ($\Delta x_u = 0.3$ nm) (ref. 5) and the unfolding rate constant determined for the third FN-III domain of tenascin ($\alpha_o = 4.6 \times 10^{-4}$ s⁻¹) (ref. 24).

Refolding of the TNfnALL protein was not instantaneous: it was important to wait several seconds between consecutive extensions for the saw-tooth pattern to be fully restored. To study this in detail, we used a double-pulse protocol where the pulse interval was varied (Fig. 4A, B). The number of FN-III domains refolded, after a complete unfolding, recovered with a double-exponential time course. Roughly 30% of the recovery occurred at a fast rate (42 s⁻¹) whereas 57% occurred at a much slower rate (0.5 s⁻¹). As we were counting the number of domains completely renatured (that is, domains capable of generating a stretch peak), these results indicate that some domains refold at the fast rate and some at the slower rate. Double-exponential refolding of FN-III domains has been observed with circular dichroism and fluorescence techniques^{6,7,24}. However, the fast refolding rates observed here are faster than those observed in chemical renaturing. For example, a value of 2.9 s⁻¹ has been found for TNfn3 (ref. 24), and values of 20 and 0.04 s⁻¹ have been found for the major, fastest folding of the FN10 and FN9 subunits, respectively, from fibronectin. Therefore, some of the domains of tenascin are refolding at more than twice the fastest rate previously reported for an FN-III domain, which were already surprisingly fast considering the presence of multiple prolines⁶. The AFM is therefore a powerful tool for studying refolding of single protein domains at a rapid timescale.

Mechanical interactions between cells involve receptor–ligand bonds, which can be challenged by forces in the range 100–200 pN during rolling adhesions^{3,4}. In these reactions, the membrane receptors and/or their matrix ligands are typically elongated, multi-domain proteins. Tenascin has been shown to bind to an as yet unknown receptor on lymphocytes to support cell rolling¹². Tenascin-dependent cell rolling is likely to trigger folding/unfolding reactions of the FN-III modular region of tenascin. The dynamic extensibility of this region could allow the tenascin–receptor bond to persist over long extensions; because the bond persists over a longer time the eventual rupture force will be lower (Fig. 5). These properties of FN-III modules may be used in other proteins containing such domains. □

Methods

Single-molecule atomic-force microscopy. Our atomic-force microscope

was constructed using a Digital Instruments (Santa Barbara, SA, USA) AFM detector head (AFM-689) mounted on top of a Physik Instrumente (Waldbronn, Germany) single-axis piezoelectric positioner (P732.ZC). Data sampling and control of the piezoelectric positioner were done by means of an AT-MIO-16X data-acquisition board driven by LabView software (National Instruments). The spring constant of each individual AFM cantilever was calibrated in solution using the equipartition theorem as described²⁵. This method gives values for the spring constant of the cantilever which are within 20% of the values obtained by other methods²⁵. Human native and recombinant tenascin-C proteins were expressed and purified as described²¹. The proteins were suspended in phosphate-buffered saline at a concentration of 10–100 µg ml⁻¹ and were allowed to adsorb onto freshly evaporated gold coverslips. Force–extension curves for single tenascin proteins were obtained under conditions similar to those used to stretch single titin proteins⁵.

Monte Carlo simulations of domain unfolding. The unfolding of a FN-III domain was represented by a two-state Markovian model with force-dependent rate constants^{5,17}. This description gives the probability of observing the unfolding of any module as $P_u = N_f \alpha \Delta t$, where N_f is the number of folded modules, α is the unfolding rate constant and Δt is the polling interval. Similarly, the folding probability was calculated as $P_f = N_u \beta \Delta t$, where N_u is the number of unfolded modules and β is the folding rate constant. The effect of an external force on the unfolding and refolding rate constants was calculated as $\alpha = \alpha_o \exp(F \Delta x_u / kT)$ and $\beta = \beta_o \exp(-F \Delta x_f / kT)$, where F is the applied force and $\Delta x_u = 0.3$ nm and $\Delta x_f = 1$ nm are the unfolding and folding distances, respectively. The rates in the absence of an applied force, $\alpha_o = 4.6 \times 10^{-4}$ s⁻¹ and $\beta_o = 3$ s⁻¹, were taken from ref. 24. However, as refolding is not observed in the presence of a force (Fig. 3A), these values of β_o and Δx_f have no impact in the simulation of a single force–extension curve. However, they become significant when simulating unfolding/refolding cycles (see below).

In order to simulate the extension of a tenascin protein, the force experienced by the FN-III modules during a ramp extension was calculated by using the WLC model with parameters identical to those obtained in Fig. 2a ($p = 0.42$ nm; $\Delta l_c = 28.5$ nm). Once the force for a given extension was determined, the probability of unfolding of any module was calculated and then each module was polled to determine its status, following the Monte Carlo approach. Using these methods we predicted the force–extension curve for a TNfnALL protein at various rates of extension and measured the average value of the resulting force peaks. Data from several simulations were pooled together and interpolated, giving the solid line shown in Fig. 3B.

Simulations of the stretching of a protein–ligand bond during cell rolling.

We simulated protein–ligand-dependent cell rolling (cell radius $r = 5$ µm; rolling velocity $v = 1$ µm s⁻¹) where a cell-bound protein is stretched along a cycloidal path (Fig. 5a, dotted line). At this rolling speed, a cell-bound protein extended by ~100 nm in length will be stretched at speeds of up to 0.2 nm ms⁻¹ (compare with values in Fig. 3b). Upon stretching, a protein–ligand bond will break under an applied force as described²⁶, where the rate of bond dissociation is given by $K_{off} = K_o \exp(F \Delta x_{bond} / kT)$. K_o is the bond off-rate in the absence of a force and Δx_{bond} is the distance over which the bond becomes unstable and fails.

To examine the effect of domain unfolding on a protein–ligand bond we simulated two mechanical arrangements: a bond with a short protein ($l_c = 50$ nm) that lacks extensible domains (Fig. 5b) and a bond with a modular protein composed of 15 FN-III domains (Fig. 5c). The bond parameters used ($\Delta x_{bond} = 0.04$ nm, and $K_o = 0.95$ s⁻¹) were those of P-selectin⁴, an extracellular protein that supports cell rolling and that is unlikely to be extensible because of its high content of disulphide bonds⁸. The force–extension relationship for the polypeptides was calculated with the WLC model ($p = 0.42$ nm; Fig. 2a). The unfolding parameters for FN-III domains were those determined for the tenascin protein (Fig. 2).

Monte Carlo simulations of a protein–ligand bond with a protein contour length of $l_c = 50$ nm (see, for example, Fig. 5b) give force–extension curves corresponding to a simple WLC, with an abrupt ending marking bond rupture. The bond ruptured after extending the protein by 40 ± 12 nm ($n = 500$); rupture forces averaged 445 ± 283 pN ($n = 500$).

In contrast, Monte Carlo simulations of a bond with a modular protein (Fig. 5c; 15 tandem FN-III domains; folded length, 50 nm) give force–extension curves with a series of force peaks forming a saw-tooth pattern that is similar to that observed experimentally here for tenascin. In this case, the bond ruptured

after extending the protein by an average of 121 ± 94 nm; rupture forces averaged 65 ± 44 pN ($n = 500$). The lower bond-rupture forces predicted in this case suggest that, during cell rolling, protein-domain unfolding can be considered to be part of the susceptibility of the kinetics of the protein-receptor bond to an applied force (reactive compliance^{4,27}).

Received 17 November 1997; accepted 20 February 1998.

1. Palecek, S. P., Loftus, J. C., Ginsberg, M. H., Lauffenberger, D. A. & Horwitz, A. F. Integrin-ligand binding properties govern cell migration speed through cell-substratum adhesiveness. *Nature* **385**, 537–540 (1997).
2. Lauffenberger, D. A. & Horwitz, A. F. Cell migration: a physically integrated molecular process. *Cell* **84**, 359–369 (1996).
3. Alon, R., Hammer, D. A. & Springer, T. A. Lifetime of the P-selectin carbohydrate bond and its response to tensile force in hydrodynamic flow. *Nature* **374**, 539–542 (1995).
4. Alon, R. *et al.* The kinetics of L-selectin tethers and the mechanics of selectin-mediated rolling. *J. Cell Biol.* **138**, 1169–1180 (1997).
5. Rief, M., Gautel, M., Oesterhelt, F., Fernandez, J. M. & Gaub, H. E. Reversible unfolding of individual titin immunoglobulin domains by AFM. *Science* **276**, 1109–1112 (1997).
6. Plaxco, K. W. *et al.* Rapid refolding of a proline-rich all- β -sheet fibronectin type III module. *Proc. Natl Acad. Sci. USA* **93**, 10703–10706 (1996).
7. Plaxco, K. W. *et al.* A comparison of the folding kinetics and thermodynamics of two homologous fibronectin type III domains. *J. Mol. Biol.* **270**, 763–770 (1997).
8. Bork, P. *et al.* Structure and distribution of modules in extracellular proteins. *Quart. Rev. Biophys.* **29**, 119–167 (1996).
9. Campbell, I. D. & Spitzfaden, C. Building proteins with fibronectin type III modules. *Structure* **2**, 333–337 (1994).
10. Erickson, H. P. Tenascin-C, tenascin-R and tenascin-X: a family of talented proteins in search of functions. *Curr. Opin. Cell Biol.* **5**, 869–876 (1993).
11. Chiquet-Ehrismann, R. Tenascins, a growing family of extracellular matrix proteins. *Experientia* **51**, 853–862 (1995).
12. Clark, R., Erickson, H. P. & Springer, T. A. Tenascin supports lymphocyte rolling. *J. Cell Biol.* **137**, 755–765 (1997).
13. Bork, P. & Doolittle, R. F. Proposed acquisition of an animal protein domain by bacteria. *Proc. Natl Acad. Sci. USA* **89**, 8990–8994 (1992).
14. Potts, J. R. & Campbell, I. D. Structure and function of fibronectin modules. *Matrix Biol.* **15**, 313–320 (1996).
15. Keller, T. C. S. Molecular bungees. *Nature* **387**, 233–235 (1997).
16. Tskhovrebova, L., Trinick, J., Sleep, J. A. & Simmons, R. M. Elasticity and unfolding of single molecules of the giant muscle protein titin. *Nature* **387**, 308–312 (1997).
17. Kellermayer, S. B., Smith, S. B., Granzier, H. L. & Bustanante, C. Folding-unfolding transitions in single titin molecules characterized with laser tweezers. *Science* **276**, 1112–1116 (1997).
18. Rief, M. *et al.* Single molecule force spectroscopy on polysaccharides by atomic force microscopy. *Science* **275**, 1295–1297 (1997).
19. Florin, E. L., Moy, V. T. & Gaub, H. E. Adhesion forces between individual ligand-receptor pairs. *Science* **264**, 415–417 (1994).
20. Radmacher, M., Fritz, M., Hansma, H. G. & Hansma, P. K. Direct observation of enzyme activity with the atomic force microscope. *Science* **265**, 1577–1579 (1994).
21. Aukhil, I. *et al.* Cell- and heparin-binding domains of the hexabrachion arm identified by tenascin expression proteins. *J. Biol. Chem.* **268**, 2542–2552 (1993).
22. Marko, J. F. & Siggia, E. D. Stretching DNA. *Macromolecules* **28**, 8759–8770 (1995).
23. Leahy, D. J., Hendrickson, W. A., Aukhil, I. & Erickson, H. P. Structure of a fibronectin type III domain from tenascin phased by MAD analysis of the selenomethionylprotein. *Science* **258**, 987–991 (1992).
24. Clarke, J., Hamill, S. J. & Johnson, C. M. Folding and stability of a fibronectin type III domain of human tenascin. *J. Mol. Biol.* **270**, 771–778 (1997).
25. Florin, E. L. *et al.* Sensing specific molecular interactions with the atomic force microscope. *Biosens. Bioelectron.* **10**, 895–901 (1995).
26. Bell, G. I. Models for the specific adhesion of cells to cells. *Science* **200**, 618–627 (1978).
27. Hammer, D. A. & Apte, S. M. Simulation of cell rolling and adhesion on surfaces in shear flow: general results and analysis of selectin-mediated neutrophil adhesion. *Biophys. J.* **63**, 35–57 (1992).

Correspondence and requests for materials should be addressed to J.M.F. (e-mail: fernandez.julio@mayo.edu).

Regulation of adenovirus alternative RNA splicing by dephosphorylation of SR proteins

Arvydas Kanopka, Oliver Mühlemann, Svend Petersen-Mahrt, Camilla Estmer, Christina Öhrmalm & Göran Akusjärvi

Department of Medical Biochemistry and Microbiology, BMC, Uppsala University, Box 582, S-751 23 Uppsala, Sweden

SR proteins are a family of essential splicing factors required for early recognition of splice sites during spliceosome assembly^{1,2}. They also function as alternative RNA splicing factors when overexpressed *in vivo* or added in excess to extracts *in vitro*^{1,2}. SR proteins are highly phosphorylated *in vivo*, a modification that

is required for their function in spliceosome assembly^{3,4} and splicing catalysis^{5,6}. Here we show that SR proteins purified from late adenovirus-infected cells are inactivated as splicing enhancer or splicing repressor proteins by virus-induced dephosphorylation. We further show that the virus-encoded protein E4-ORF4 activates dephosphorylation by protein phosphatase 2A of HeLa SR proteins and converts their splicing properties into that of SR proteins purified from late adenovirus-infected cells. Taken together, our results suggest that E4-ORF4 is an important factor controlling the temporal shift in adenovirus alternative RNA splicing. We conclude that alternative pre-mRNA splicing, like many other biological processes, is regulated by reversible protein phosphorylation.

The adenovirus L1 unit⁷ is an alternatively spliced pre-mRNA in which a common 5' splice site can be joined to two alternative 3' splice sites, resulting in the production of the 52,55K (proximal 3' splice site) or the IIIa (distal 3' splice site) mRNA. During a lytic adenovirus infection, L1 alternative RNA splicing is temporally regulated, such that efficient IIIa 3' splice-site usage is confined to the late phase of virus infection⁷. We have previously shown that IIIa splicing is repressed in uninfected HeLa cell nuclear extracts (HeLa-NE) by SR proteins binding to an intronic repressor element (the 3RE)⁸ located immediately upstream of the IIIa 3' splice site.

Removing the 3RE element from a mini-52,55K–IIIa tandem transcript⁸ mimics the early to late shift in L1 alternative splicing observed *in vivo* (data not shown), emphasizing that inhibition of IIIa splicing by SR proteins is important for L1 alternative 3' splice-site usage. The steady-state amount of the classical SR proteins⁹ does not change significantly during virus infection (data not shown), suggesting that the shift to increased IIIa splicing late in infection results from a virus-induced inactivation of the repressor function of SR proteins. To test this hypothesis, we compared the biological activity of SR protein from uninfected HeLa cells (SR-HeLa) and late adenovirus-infected cells (SR-Ad). Addition of excess SR-HeLa to HeLa-NE efficiently repressed IIIa splicing (Fig. 1a)⁸, whereas adding the same amount of SR-Ad to HeLa-NE resulted in only a moderate inhibition of IIIa splicing. Also, addition of SR-Ad to splicing-deficient HeLa S100 extracts¹⁰ resulted in a much smaller activation of 52,55K splicing than SR-HeLa (Fig. 1b). These results suggest that SR-Ad proteins are no longer able to function efficiently as a splicing repressor or splicing enhancer proteins, most probably as a result of losing their RNA-binding capacity (Fig. 1c). However, this reduced capacity to bind RNA does not result from a co-purification of late adenovirus RNA (data not shown), indicating that L1 splicing is not regulated by the sequestering model suggested to control E1A alternative RNA splicing¹¹.

To investigate whether the decreased activity of SR-Ad in splicing regulation and RNA binding (Fig. 1) correlated with a change in phosphorylation, *in vivo* ³²P-labelled SR-HeLa and SR-Ad proteins were analysed by two-dimensional gel electrophoresis (Fig. 2). Two differences were consistently observed in multiple experiments. First, total incorporation of ³²P into SR-Ad was significantly reduced compared with SR-HeLa. Second, with the exception of SRp20, the isoelectric point of a large fraction of the SR-Ad proteins was significantly shifted towards the basic side of the gel, suggesting that SR-Ad are underphosphorylated. That the major ³²P-labelled proteins (Fig. 2) are SR proteins was confirmed by mAb104 (ref. 12) staining of western blots (data not shown).

The adenovirus protein E4-ORF4 associates with the serine- and threonine-specific protein phosphatase 2A (PP2A)¹³. The E4-ORF4-PP2A complex has previously been suggested to regulate transcription by inducing dephosphorylation of specific transcription factors^{14,15}. To test whether E4-ORF4 also controls RNA splicing, we sought to convert the splicing properties of SR-HeLa to that of SR-Ad. Incubation of ³²P-labelled SR-HeLa in HeLa-NE in the presence of recombinant E4-ORF4 resulted in increased phosphate release compared with HeLa-NE alone (Fig. 3a). Inclusion of